Batteries & Supercaps

Articles
doi.org/10.1002/batt.202000007

Chemistry Europe
European Chemical
Societies Publishing

Interlayer Engineering of MnO_2 with High Charge Density Bi^{3+} for High Rate and Stable Aqueous Supercapacitor

Ting Xiong,[a, b] Mingke Zhu,[a] Yaoxin Zhang,[a] Wee Siang Vincent Lee,*[a] Zhi Gen Yu,*[c] and Junmin Xue*[a]

Two-dimensional δ-MnO_2 has attracted considerable attention as supercapacitor electrode due to its ability to incorporate foreign ions into its interlayer spacing which suggests the possibility of capacitance enhancement through interlayer engineering. Incorporating high charge density cation such as Bi^{3+} into the MnO_2 interlayer becomes an attractive strategy that not only serves to stabilize the layer structure, it is also an important prelude towards the weakening of the chemical bonding between the O from MnO_2 and the intercalating electrolyte species. This in turn leads to higher reversibility while ensuring excellent structural stability that is portrayed in enhanced cyclic stability and rate performance. Herein, the

Bi^{3+}-modified δ-MnO_2 delivered a reversible specific capacity of 421 F g^{-1} at 1 A g^{-1}, which is higher than that of the previously reported mono/divalent cation-intercalant modified MnO_2 systems. Using the N-doped carbon nanosheets as the negative electrode, the assembled asymmetric supercapacitor achieved a high capacitance of 77 F g^{-1} at 1 Ag^{-1}. Furthermore, the high energy density of 20 Wh kg^{-1} was recorded at a high-power density of 39 kW kg^{-1}, while simultaneously demonstrating excellent cycle performance of 82 % capacitance retention after 40 000 cycles. This work has shown that interlayer engineering of layered MnO_2 could potentially provide new insight into the development of high-performance supercapacitor electrode.

1. Introduction

Designing electrode material is deemed as one of the vital strategies towards the development of high-performance energy storage devices such as supercapacitor,[1–4] and batteries.[5,6] For instance, the most widely investigated supercapacitor electrode material is the manganese oxide (MnO_2) due to its numerous crystalline polymorphs. Recently, it was shown that the performance of the MnO_2 electrode is strongly dependent on the crystallographic structure, in the order of $\alpha \approx \delta > \gamma > \lambda > \beta$-$MnO_2$.[7–13] This phenomenon inadvertently leads to the increasing research interests in α- and δ-MnO_2 due to the promise of their higher capacitances. Between these two polymorphs, δ-MnO_2 is particularly interesting due to its infinite two-dimensional sheets of edge-shared {$Mn^{IV}O_6$} octahedra structure separated by an interlayer spacing of 0.7 nm.[14,15] Such layered structure is exciting as it can incorporate foreign

ions into its interlayer spacing, which suggests the possibility of potential electrochemical performance enhancement through interlayer engineering.[16,17]

In an attempt to leverage on interlayer engineering to modify the performance of δ-MnO_2, various intercalant cations such as Ag, Ba, Ca, Ce, Cu, K, La, Pb, Sb, Sn, Y and Zn have been incorporated into the material.[18–23] Based on the studies, the incorporation of cations into the interlayer spacing of δ-MnO_2 could aid in the inhibition of significant volumetric changes and this process could effectively prevent the collapse of the open structure. Such duality not only enhances the cyclic stability, and it could potentially improve the rate performance of δ-MnO_2. The key mechanism for the electrochemical performance enhancement is largely due to the polarization of the electron cloud of the O from MnO_2 by the cations that were introduced into the interlayer spacing. Such polarization in turn causes the electron cloud of the neighboring O to be distorted away from the intercalating electrolyte species, and hence enhancing the reversibility of the insertion/extraction process of these species. However, most of the intercalant cations used in the interlayer engineering of δ-MnO_2 typically possess low charge density which could lead to 2 possible issues; (1) the lower structural stabilization effect, and (2) the smaller extent of electron cloud polarization of the neighboring O which in turn form a greater electrostatic attraction with the intercalating electrolyte species. Thus, even though low charge density cations could generally enhance the performance of δ-MnO_2, their impacts are still significantly masked. As a result, most of the monovalent/divalent cation intercalant modified MnO_2 systems were only able to report capacitances of 200–300 F g^{-1}[24–29] which, even though are higher as compared to pristine MnO_2 (ca. 200 F g^{-1}),[30] remain to be unsatisfactory. Hence, in order to address such limitations, it is

[a] T. Xiong, M. Zhu, Dr. Y. Zhang, Dr. W. S. V. Lee, Prof. J. Xue
National University of Singapore
Department of Materials Science and Engineering
Singapore, Singapore 117573
Fax: (+65) 65164655
E-mail: mseleew@nus.edu.sg
msexuejm@nus.edu.sg
[b] T. Xiong
Centre for Advanced 2D Materials and Graphene Research Centre
National University of Singapore
Singapore 117546
[c] Prof. Z. G. Yu
Institute of High Performance Computing
Singapore 138632
E-mail: yuzg@ihpc.a-star.edu.sg

Supporting information for this article is available on the WWW under https://doi.org/10.1002/batt.202000007

highly necessary to utilize high charge density cations as the intercalants for δ-MnO$_2$.

Bismuth (Bi) is an attractive material due to its low cost and non-toxic nature.[31,32] As Bi typically exists as 3 +, it possesses high charge density that could potentially distort the O electron cloud more effectively as compared to most of its metal cations counterpart. Herein, Bi^{3+} intercalated δ-MnO$_2$ was prepared via a facile electrochemical deposition method and it was used as the positive electrode. The Bi^{3+}-modified δ-MnO$_2$ delivered a reversible specific capacity of 421 F g^{-1} at 1 A g^{-1}, which is higher than that of the previously reported mono/divalent cation-intercalant modified MnO$_2$ systems. To complement it, N-doped carbon nanosheet was used as the negative electrode. In an asymmetric supercapacitor configuration, the device was able to deliver a high capacitance of 77 F g^{-1} at 1 A g^{-1} with an energy density 20 Wh kg^{-1} at the power density of 39 kW kg^{-1}. In particular, excellent cyclic stability was recorded with an 82% capacitance retention after 40 000 cycles at a current density of 10 A g^{-1}. The improvement in the electrochemical performance could stem from the benefits of Bi^{3+} intercalant in the MnO$_2$ interlayer spacing; (1) Bi^{3+} could stabilize the layer structure due to the strong hybridization between Bi and O from MnO$_2$, (2) greater reversibility of Na$^+$ insertion/extraction into/out of the MnO$_2$ lattice (hence, renewed active area), and (3) the increased conductivity. Thus, this work has shown significant promise in modifying the electrochemical performance of the electrode by incorporating intercalants (e.g. Bi^{3+}) into layered materials (e.g. MnO$_2$). Furthermore, it is shown in this work that the weakening of interaction between electrolyte species with O from MnO$_2$ is the primary reason for such performance enhancement.

2. Results and Discussion

2.1. Material Characterization of Bi^{3+}-modified MnO$_2$ Nanosheets

To realize Bi^{3+} intercalated MnO$_2$ for the investigation, Bi^{3+}-modified MnO$_2$ were synthesized via a simple electrodeposition method. Unmodified MnO$_2$ was prepared as a control via the same method but it was conducted without a bismuth source. The crystal structures of the as-synthesized samples were studied by X-ray diffraction (XRD) test and the results were recorded and shown in Figure 1a. All the diffraction peaks of MnO$_2$ and Bi^{3+}-modified MnO$_2$ could be indexed to the birnessite MnO$_2$ (denoted as δ-MnO$_2$) (JCPDS No. 13-0105). However, the diffraction peak of carbon resulting from the carbon cloth was also observed which suggests that samples with birnessite structure were successfully grown onto the carbon cloth surface. Interestingly the peak at 12.1° shifted to a lower angle for Bi^{3+}-modified MnO$_2$ as compared to its unmodified counterpart, which corresponds to a slight increase of interlayer distance from ~0.72 nm for MnO$_2$ to ~0.77 nm for Bi^{3+}-modified MnO$_2$. The shift in the angle may be attributed to the widening of the interlayer spacing due to the incorporation of Bi^{3+}.[33]

Morphologies of the as-synthesized samples were studied using scanning electron microscopy (SEM) and transmission electron microscopy (TEM). As shown in Figure 1b and Figure S1a, the as-prepared MnO$_2$ samples densely wrapping and uniformly anchoring on the carbon cloth presented sheet-like morphology. TEM was further utilized to investigate the sheet-like morphology as shown in the inset of Figure 1b. A typical edge-view of the MnO$_2$ nanosheet with clear lattice fringes is shown in HRTEM image. The interplanar spacing of 0.70 nm corresponds to the (001) plane of birnessite MnO$_2$. The as-prepared Bi^{3+}-modified MnO$_2$ also showed sheets-like morphology, which is similar to the MnO$_2$ (Figure 1c and Figure S1b).
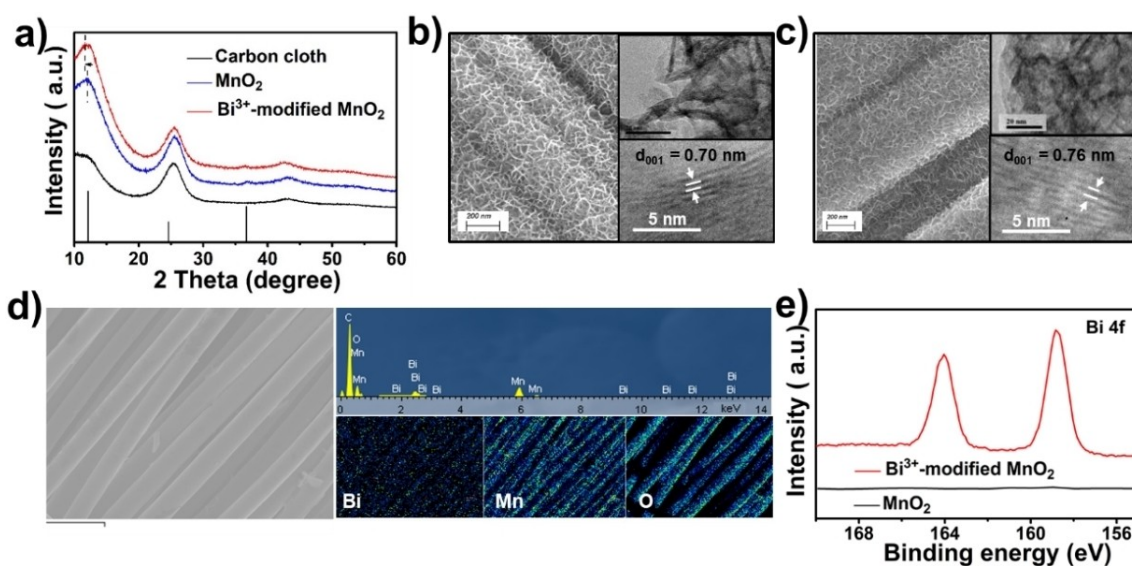

Figure 1. a) XRD patterns, b) SEM and TEM images of MnO$_2$, c) SEM and TEM images of Bi^{3+}-modified MnO$_2$, d) EDX-Mapping of Bi^{3+}-modified MnO$_2$, e) Bi 4f XPS of MnO$_2$ and Bi^{3+}-modified MnO$_2$.

For the HRTEM image in the inset of Figure 1c, wider d-spacing of ca. 0.76 nm was recorded which could be a result of the intercalation of Bi^{3+} ions into the MnO_2 interlayers. These HRTEM images results are consistent with the XRD results which both suggest the expanded interlayer spacing due to the successful Bi^{3+} intercalation. Energy-dispersive X-ray (EDX) spectrum mapping (Figure 1d) revealed well distribution of Mn, O, and Bi elements within the nanosheets, which further confirms the successful introduction of Bi^{3+} into MnO_2.

The chemical composition and surface states of Bi^{3+} modified MnO_2 and its unmodified counterpart were studied with X-ray photoelectron spectroscopy (XPS). In Figure S2a, the XPS full survey spectrum of Bi^{3+}-modified MnO_2 indicates the presence of Mn, O, C, and Bi elements, further indicating the successful introduction of Bi^{3+} ions into MnO_2. As shown in Figure 1e, two strong peaks at 164.0 and 158.8 eV corresponding to $Bi4f_{5/2}$ and Bi $4f_{7/2}$ could be observed for the Bi^{3+}-modified MnO_2 sample. These signals could be attributed to Bi^{3+}, indicating that Bi that is presented is in the valence of $+3$.[34] High-resolution Mn 2p spectra (Figure S2b) exhibited two peaks with energy separation of 11.7 and 11.9 eV for MnO_2 and Bi^{3+}-modified MnO_2, respectively, which suggests the slight decrease in the Mn oxidation state for Bi^{3+}-modified MnO_2 as compared to that of MnO_2. The ICP analysis demonstrated a ratio of Bi to Mn of about 0.2, which further confirmed that Bi ion is introduced into the MnO_2. Thus, based on the collective results from XRD, TEM, XPS, and ICP, it is suggested that Bi^{3+} could be incorporated into the MnO_2 interlayer.

2.2. Electrochemical Characterization of Bi^{3+}-modified MnO_2 Nanosheets

Electrochemical performances of MnO_2 and Bi^{3+}-modified MnO_2 nanosheets were investigated using a three-electrode system in 1 M Na_2SO_4 aqueous electrolyte. Figure 2a shows the cyclic voltammetry (CV) curves of the two samples in a potential window of 0 to 1.3 V vs. SCE at a scan rate of 25 mV s^{-1}. Due to the significant oxygen evolution reaction (OER), MnO_2 was unable to operate in the potential window of 0–1.3 V. Interestingly, Bi^{3+}-modified MnO_2 was able to operate the same potential window without demonstrating OER activity. Figure 2b exhibits the galvanostatic charge and discharge (GCD) curves of the MnO_2 and Bi^{3+}-modified MnO_2 electrodes at a current density of 1 A g^{-1}. Apparently, OER has occurred for the MnO_2 electrode, which is consistent with the CV curve. Prior reports have reported intercalating the δ-MnO_2 layered structure with ions like Na^+ and K^+ could aid in improving the electrochemical characteristics and increasing the onset potential for OER.[28,29] Herein, similarly, after Bi^{3+} modification, the oxygen evolution reaction was shown to be suppressed.

Figure 2c exhibits GCD curves of the Bi^{3+}-modified MnO_2 electrodes at different current densities. The charge time was almost similar to the discharge time, which suggests the reversibility of the Bi^{3+}-modified MnO_2 electrode materials. The specific capacitance of Bi^{3+}-modified MnO_2 reached 421 F g^{-1} (areal capacitance of 0.53 F cm^{-2}) at a current density of 1 A g^{-1}, which is higher than most reported MnO_2 to date (summarized in Table S1). A respectable capacitance of 200 F g^{-1} was still achieved as the current density increased 50 times, indicating the good rate performance (Figure 2d). However, for the MnO_2, lower capacitance of 370 F g^{-1} at 1 A g^{-1} was recorded with rapid capacitance
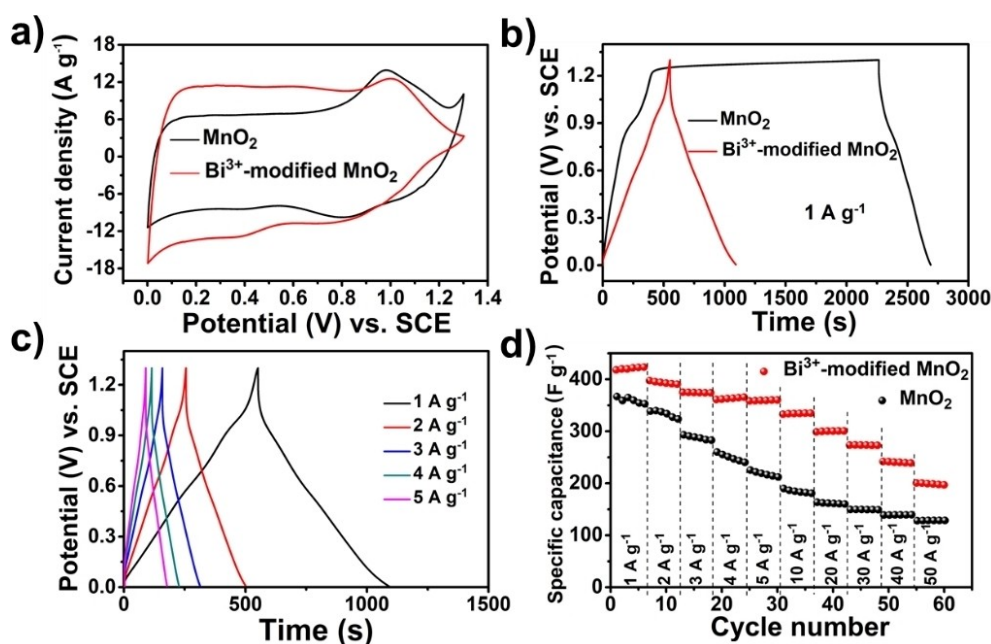

Figure 2. a) Typical CV curves and b) galvanostatic charge and discharge curves of MnO_2 and Bi^{3+}-modified MnO_2, c) galvanostatic charge and discharge curves of Bi^{3+}-modified MnO_2 and d) Rate performances of MnO_2 and Bi^{3+}-modified MnO_2.

Batteries & Supercaps

Articles
doi.org/10.1002/batt.202000007

Chemistry Europe
European Chemical
Societies Publishing

fading due to the oxygen evolution reaction. Notably, the irreversible capacitance percentage loss between the first-second cycle was about 2% for MnO_2 while negligible loss was observed for Bi^{3+}-modified MnO_2. Such result may suggest the greater reversibility of Na^+ insertion/extraction for Bi^{3+}-modified MnO_2 as compared to its unmodified counterpart due to the weakening of O and Na^+ bond by the strong hybridization of Bi and O. Thus, the Na^+ propagation barrier is largely reduced, resulting in high mobility of the intercalating Na^+. Hence based on the electro-chemical performance result, Bi^{3+} modified MnO_2 electrode showed wider potential window, enhanced capacitance, and greater reversibility.

2.3. Material Characterization of N-doped Carbon Nanosheets

To complement the Bi^{3+}-modified MnO_2, N-doped carbon (labeled as NDC) nanosheets were synthesized by a simple calcining method. The morphology and microstructure of N-doped carbon was characterized by SEM and TEM. Nanosheet structures were clearly identifiable in SEM and TEM images (Figure 3a and 3b). The as-prepared carbon inherited similar morphology as g-C_3N_4 precursor (Figure S3), suggesting that g-C_3N_4 nanosheets acted as template to guide the growth of the carbon nanosheets. In the inset of Figure 3b, amorphous feature of the N-doped carbon could be observed by a typical ring feature. In the Raman spectrum (Figure 3c), two peaks located at 1341 and 1596 cm^{-1} were assigned to the D-band and G-band of carbon, separately. The intensity of D band to G band (0.5) confirms a graphitic structure.[35]

The chemical elements in the as-prepared carbon nano-sheets were confirmed by the element signals of C, N and O in the XPS survey spectrum (Figure 3d). The N 2p spectrum in Figure 3e confirms that the sample was N doped, with the N content determined to be 6.8 at%. The peaks at 398 and 400.5 eV were assigned to pyridinic N and pyrrolic N, respectively, while the ones centered at 402.4 and 405.3 eV, which were ascribed to the quaternary N and the pyridine-N-oxide species, respectively.[35] The introduction of nitrogen could aid in enhancing the wettability and conductivity of carbon, while simultaneously provides pseudocapacitance contribution through the surface redox reactions, thus resulting in high capacitance.[36] As revealed by the nitrogen adsorption-desorption isotherms, NDC possessed a Brunauer-Emmett-Teller (BET) specific surface area of 327.6 $m^2 g^{-1}$. The hysteresis loop of the isotherm indicated the existence of mesopores, and the pore size distributions were mainly at ~5 nm (Figure 3f). These pore structures allow short diffusion paths and rapid electron transport, resulting in good supercapacitive perform-ances. These results confirmed that N-modified carbon nano-sheets with rich porous structure were successfully synthesized.

2.4. Electrochemical Characterization of N-doped Carbon Nanosheets

The electrochemical properties of NDC were first measured by CV test in 1 M $NaSO_4$ electrolyte in the potential range from −1.2 to 0V (vs. SCE) at 25 mV s^{-1}. The CV curve in Figure S4 displayed a relatively rectangular shape, implying capacitive behavior. The CV curve area also increases with the scan rate increase (Figure 4a). Meanwhile, the CV curves maintain similar shapes, indicating the excellent structure stability of carbon electrode material. Figure 4b shows the GCD curves of NDC at different current densities, and the GCD curves exhibited typical triangular shapes with a slightly distorted line that could be caused by the presence of pseudocapacitance from N doping.[37] Notably, a negligible voltage drop was observed at the discharge process, confirming the low internal resistance of NDC. As shown in Figure 4c, NDC could deliver a specific capacitance of 225 F g^{-1} at the current
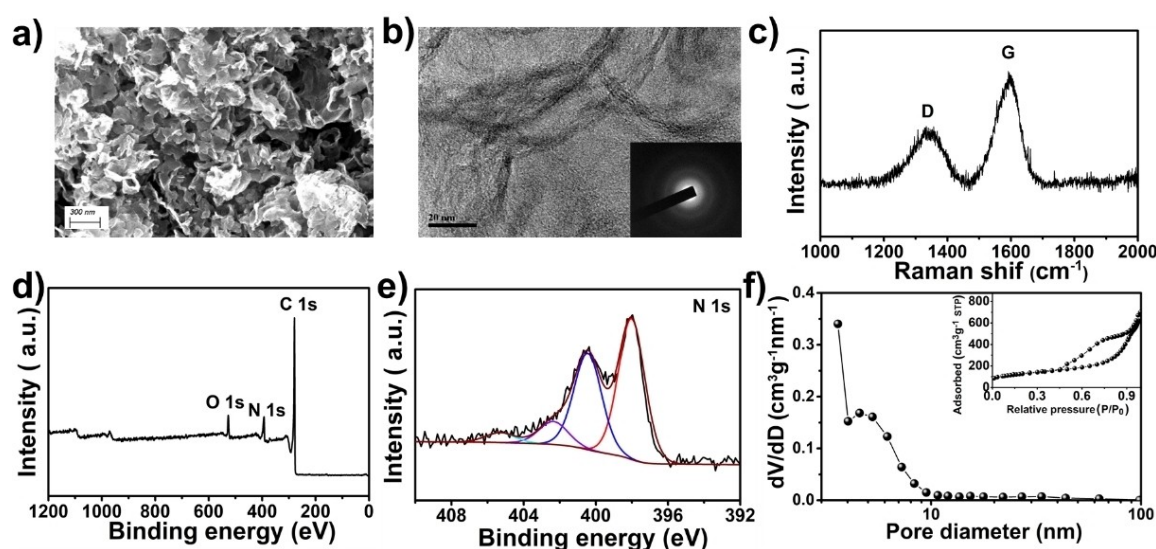

Figure 3. a) SEM image, b) TEM image, c) Raman spectrum, d) XPS survey spectrum, e) N1s XPS spectrum, f) pore size distribution plot (Nitrogen adsorption-desorption isotherm) of NDC.
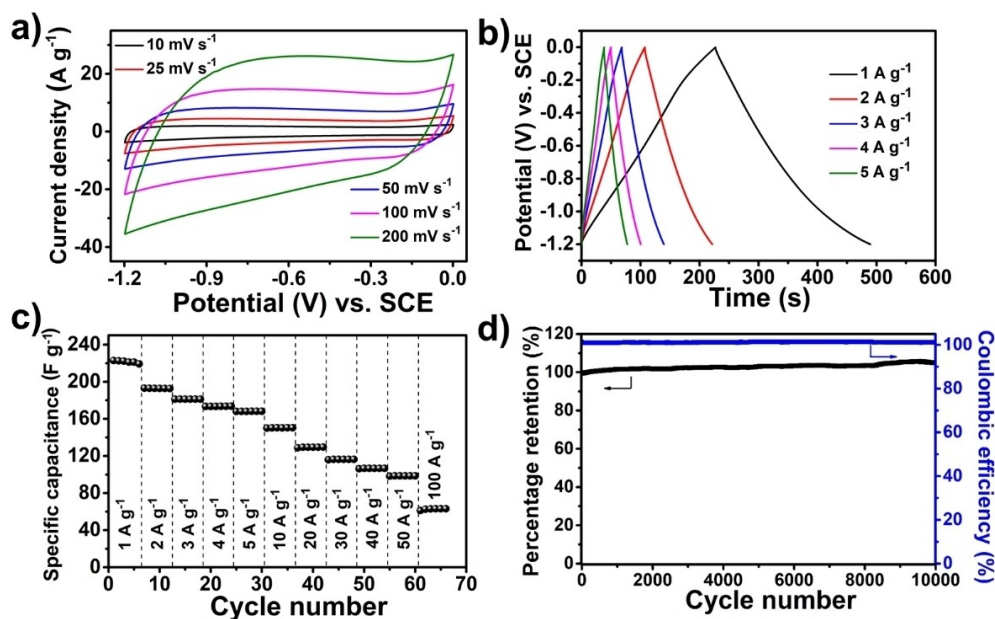
Batteries & Supercaps

Articles
doi.org/10.1002/batt.202000007

Chemistry Europe
European Chemical
Societies Publishing

Figure 4. a) CV curve, b) GCD curves, c) rate performance, d) cycling performance at the current density of $10\,A\,g^{-1}$ of the NDC.

density of $1\,A\,g^{-1}$. The capacitance retention is 47.6% when the current density varies from $1\,A\,g^{-1}$ to $50\,A\,g^{-1}$, indicating the superior rate capability. The good cycling stability of the carbon electrode materials is demonstrated by the 100% capacitance retention and 100% Coulombic efficiency after 10 000 charge-discharge cycles at a high current density of $10\,A\,g^{-1}$ (Figure 4d).

2.5. Electrochemical Performance of the Bi^{3+}-modified MnO_2//NDC Supercapacitor

An asymmetric supercapacitor was assembled with Bi^{3+}-modified MnO_2 as the positive electrode and NDC as the negative electrode. Figure S5 exhibits the CV curves of Bi^{3+}-modified MnO_2 and NDC electrodes, and their operating potential windows were 0–1.3 and -1.2–0 V, respectively, which suggests a possible 2.5 V for the full cell. The CV curves for the asymmetric supercapacitor were then tested between 0 to 2.5 V with scan rates from 10 to $200\,mV\,s^{-1}$ as shown in Figure 5a. The CV curves retain similar shapes even when the scan rate increase to $200\,mV\,s^{-1}$, indicating the fast charge and discharge capability of the assembled supercapacitor. This behavior agrees well with the GCD measurements charging/discharge performances tested at various current densities (Figure 5b). The specific capacitance could reach $77\,F\,g^{-1}$ at a current density of $1\,A\,g^{-1}$. A remarkable rate performance has been achieved by the as-obtained supercapacitors, which maintained about 49.8% of the initial capacitance as current density increased from 1 to $50\,A\,g^{-1}$ (Figure 5c).

The power densities and energy densities are shown in Figure 5d. A maximum energy density of $63\,Wh\,kg^{-1}$ at a power density of $1176\,W\,kg^{-1}$ was achieved, and a maximum power density of $39\,kW\,kg^{-1}$ with an energy density of $20\,Wh\,kg^{-1}$, which is superior to that previously reported.[28,29] Figure 5e shows that 82% capacitance retention of the device is observed after 40 000

cycles, which indicates its excellent cycle performance. Also, the as-prepared Bi^{3+}-modified MnO_2 is stable. As shown in Figure S6, the cycled Bi^{3+}-modified MnO_2 showed similar XRD and SEM results to the fresh one. The good stability could be attributed to Bi^{3+} ions, which located at the interlayer to provide the "elasticity" necessary for the MnO_2 lattice to sustain a good reversibility of the redox reaction.[38] Whereas for the MnO_2//NDC supercapacitor, obvious oxygen evolution reaction was observed as shown in Figure S7 with the similar potential window. Furthermore, with this potential window, the stability was significantly poorer as the supercapacitor was inoperable after 5000 cycles.

To gain an in-depth understanding of the correlation between Bi^{3+} modification and the enhanced electrochemical performance, we performed the first principles simulations to study electrical properties of pristine and Bi^{3+}-modified MnO_2 containing an embedded Na ion. As shown in Figure 6a, without the presence of Bi^{3+} intercalant in MnO_2, Na^+ was able to form strong bonding with the neighbouring O from MnO_2. However, with the introduction of Bi^{3+}, significant electron transfer was observed between Bi and O due to strong hybridization (Figure 6b). This could stabilize the layer structure. According to the results of the partial density of states (PDOS) (Figure 6c), p orbital of Bi is strongly hybridized with s and p orbitals of O. This strong hybridization subsequently weakens the chemical bonding between the intercalating electrolyte species (e.g. Na^+ in Na_2SO_4) with O from MnO_2. The reduction in chemical bond strength between O and Na^+ in turn suggests greater reversibility in terms of insertion/extraction process during charge/discharge. Thus, due to the constantly renewed sites, close to the similar amount of Na^+ will be able to be inserted into the interlayer and thus cyclic stability is enhanced. Furthermore, due to the incorporation of the Bi^{3+} intercalant, the system conductivity could be enhanced due to the donation of 1.895 electrons each Bi^{3+} obtained from Bader charge calculations.
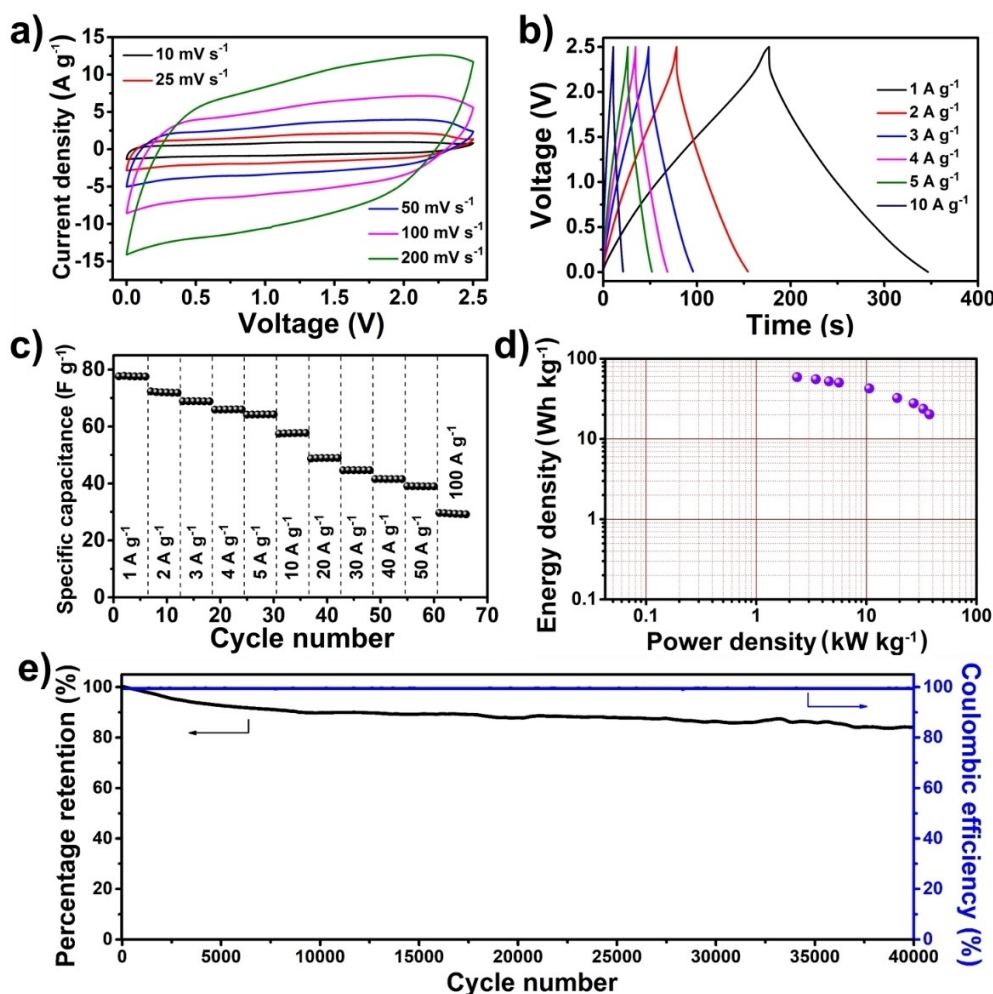
Figure 5. a) CV curves of Bi^{3+}-modified MnO_2//NDC supercapacitor, b) charge/discharge curves, c) rate performances, d) Ragone plot, e) cycling performance and Coulombic efficiency at the current density of $10\,A\,g^{-1}$.
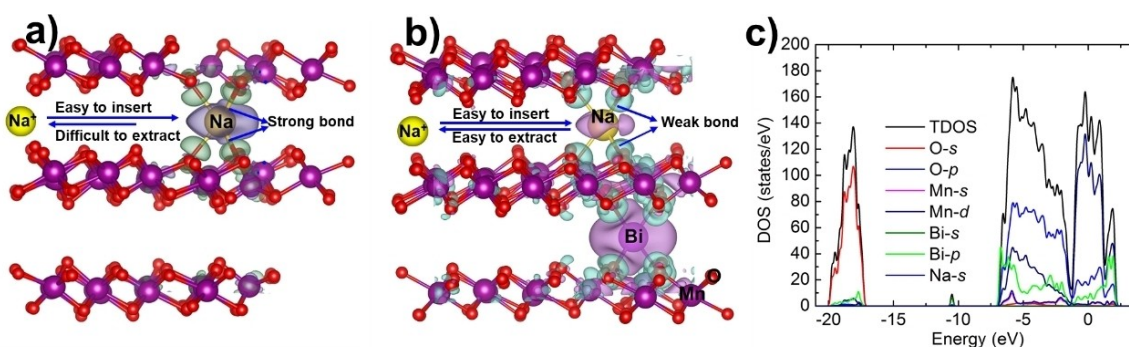

Figure 6. Charge difference distribution of Na^+ in the interlayer of MnO_2 a) without and b) with Bi^{3+} modification (The light purple represents electron depletion, and green represents electron accumulation), c) partial density of states of Bi^{3+}-modified MnO_2 with Na^+ in the layer structure.

To provide a better understanding of Bi^{3+} modification to the electrochemical performance, the electrochemical active surface area was calculated by measuring the capacitive current involved with double layer charging from the scan-rate dependence of cyclic voltammetry (Figure S8 and Figure S9). By plotting the difference in current density (J) between anodic and cathodic sweeps (ΔJ) at a fixed potential against the scan rate, a linear trend would be observed. The fitting slope was twice of the double-layer capacitance (C_{dl}), which is linearly proportional to the electrochemical active surface area.[39] The Bi^{3+}-modified MnO_2 could deliver higher electrochemical active surface area of $65.5\,mF\,mg^{-1}$ than that of the MnO_2 ($45.5\,mF\,mg^{-1}$), indicating

Batteries & Supercaps

Articles
doi.org/10.1002/batt.202000007

Chemistry Europe
European Chemical
Societies Publishing

that Bi^{3+} modification could potentially renew the active areas for the storage of Na^+ ions. Besides, electrochemical impedance spectroscopy (EIS) analyses were further performed to understand the ion transport properties in the electrode–electrolyte interface. The Bi^{3+}-modified MnO_2//NDC and MnO_2//NDC supercapacitors both show one semicircle associated with the charge transfer resistance on electrode/electrolyte interface (R_{ct}) and a sloping low-frequency line, known as Warburg impedance, featuring the resistance about diffusion of ions into the active material of the electrode (Figure S10).[40] In the equivalent circuit, by fitting, Bi^{3+}-modified MnO_2 showed resistance of R_s (equivalent series resistance, 0.687 Ω), R_{ct} (charge transfer resistance, 0.944 Ω) and Z_W (10.23 Ω), much lower than those of the MnO_2 ($R_s = 0.704$ Ω, $R_{ct} = 1.593$ Ω and $Z_W = 34.1$ Ω), revealing high conductivity and very low internal resistance of the Bi^{3+}-modified MnO_2 material. Thus, based on the simulation results and experiments results, the Bi^{3+} modification not only enhance the capacitance by increasing the active area and reducing the Na^+ propagation barrier, but also enhance the stability by providing the "elasticity" necessary for the δ-MnO_2 lattice and improving the conductivity.

3. Conclusions

Bi^{3+}-modified δ-MnO_2 nanosheet was successfully grown onto carbon cloth via a facile electrochemical route. Bi^{3+} ions incorporated into the interlayer spacing not only minimized the magnitude of structural changes to improve its reversibility and cyclic stability, but also actively renew the active areas and reduced the Na^+ propagation barrier to increase the capacitance. Also, enhanced conductivity induced by Bi^{3+} modification accelerated the charge transfer processes. As expected, the as-assembled Bi^{3+}-modified δ-MnO_2//NDC asymmetric supercapacitor exhibited high energy density up to 63 Wh kg^{-1} and a power density up to 39 kW kg^{-1} and 83% of its capacitance retention after 40000 cycles. The outstanding capacitance and cyclic performance benefited interlayer engineering, i.e. Bi^{3+} modification in this work could provide new insight into the design high performance aqueous supercapacitor.

Experimental Section

Materials and methods

Materials

Urea (99.99%), glucose (≥98.5%), sodium sulfate, manganese(II) nitrate tetrahydrate, and bismuth (III) nitrate pentahydrate were purchased from Sigma-Aldrich. Carbon cloth was purchased from CeTech Company (Taiwan).

Synthesis of MnO_2 nanosheets and Bi^{3+}-modified MnO_2 nanosheets

To prepare Bi^{3+}-modified MnO_2 nanosheets, an electrochemical deposition technique was used. Carbon cloth was heat-treated at 500 °C for 1 h before use. Then, Bi^{3+}-modified MnO_2 nanosheets

were electrodeposited onto carbon cloth in a two-electrode cell, with carbon cloth as the working electrode and graphite paper as the counter electrode. The electrolyte was prepared by dissolving 0.1 M manganese nitrate tetrahydrate and 0.1 M bismuth nitrate pentahydrate into 2 M HNO_3 solution. Electrochemical deposition was performed under galvanostatic conditions at a constant current of 6 mA cm^{-2} and 5 min was used for synthesis. MnO_2 nanosheets were prepared at the same condition without the addition of bismuth nitrate pentahydrate. The deposited carbon cloth was rinsed with dilute nitrate and deionized water for several times, and dried at 60 °C for further use.

Synthesis of N-doped carbon nanosheets

The synthesis of N-doped carbon nanosheets was modified by a reported method.[41] g-C_3N_4 was fabricated by a common method (10 g of urea was heated in a muffle furnace at 500 °C for 2 h), which was used as the N-doping source and template. Then, g-C_3N_4 (0.5 g) was firstly mixed with 50 mL deionized water and sonicated for 30 min. Glucose (3 g) was added into above suspension, and was under vigorous agitation for 30 min. The mixture was then transferred to a 100 mL Teflon autoclave, and heated at 180 °C for 5 h in an oven. The product was collected by centrifugation, washed with deionized water and ethanol, and then dried in an oven at 80 °C overnight. The resulting product was heat-treated in a tubular furnace at 800 °C for 4 h under N_2 atmosphere with a heating rate of 5 °C min^{-1}. The final product was labeled as NDC.

Characterization

The powder X-ray diffraction (XRD) pattern was measured by a powder diffractometer (Bruker D8 Advanced Diffractometer System) with a Cu Kα (1.5418 Å) source. Scanning electron microscopy (SEM) images were recorded on a ZEISS SEM Supra 40 (5 kV). Transmission electron microscopy (TEM) was performed on a JEOL-3010 (300 kV acceleration voltage). TEM samples were prepared by dripping the sample solutions onto a copper grid. Surface composition was studied by X-ray photoelectron spectroscopy (XPS) using a Kratos Analytical Axis UltraDLD UHV spectrometer with a monochromatized Al Ka X-ray source (1486.6 eV) scanning a spot size of 700 μm by 300 μm. The Brunauer-Emmett-Teller surface area was measured using the Micromerities ASAP 2020 Surface Area and Porosity Analyzer. Element analysis was performed by the ICP-optical emission spectroscopy. Raman spectrometry was conducted on a Horiba MicroRaman HR Evolution System using an argon laser beam with an excitation wavelength of 514.5 nm.

Computational methods

The first principles simulations were carried out using density-functional theory with the generalized Perdew-Burke-Ernzerhof (PBE)[42] using projector augmented wave potentials as implemented in the VASP.[43,44] The convergence for energy was chosen as 1× 10^{-7} eV between two consecutive steps, and the maximum Hellmann-Feynman forces acting on each atom were less than 0.001 eV. For MnO_2 optimization, 8×8×10 k-point samplings considering the spin polarization were used. Based on our optimized MnO_2, we expanded to 5×5×1 and tested both the substitution site and interlayer doping sites for Bi. Related results show that the most stable relaxed configuration is the interlayer doping pattern of Bi. Then we analyzed the differences in spatial charge distribution of Na^+ in the interlayer of MnO_2 with/without Bi^{3+} modification. The density of states (DOS) of Na^+ in the interlayer of Bi-modified MnO_2 was also calculated. The supercell lattice constants were fixed, and all atomic coordinates relaxed until atomic force on each atom was less than 0.001 eV Å^{-1}.

Batteries & Supercaps

Articles
doi.org/10.1002/batt.202000007

Chemistry
Europe

European Chemical
Societies Publishing

The plane-wave cut-off was tested by varying the parameter between 400 and 600 eV. Convergence to within 0.01 eV was achieved with a cut off energy of 450 eV. The Bader method[45] was used to analyze the electronic structure and the charge state of Bi ion in MnO_2.

Electrochemical measurements

All electrochemical tests were tested using an electrochemical station (Bio-logic VMP 3) at room temperature. The as-prepared MnO_2 nanosheets and Bi^{3+}-modified MnO_2 nanosheets grow on carbon cloth were directly used as electrodes. The N-doped carbon (NDC) nanosheets were mixed with carbon black and polyvinyl difluoride in an 8:1:1 weight ratio with N-methyl-2-pyrrolidone. The mixture was hand-grinded and then coated onto the carbon cloth, and finally dried at 80 °C for further use. The mass loadings for MnO_2, Bi^{3+}-modified MnO_2 or NDC are in the range of 1–2.5 mg cm^{-2}. In the three-electrode system, MnO_2, Bi^{3+}-modified MnO_2 or NDC was used as the working electrode, saturated calomel electrode (SCE) was used as the reference electrode, platinum plate was served as the counter electrode, and 1 M Na_2SO_4 was the electrolyte, respectively. The asymmetric supercapacitors were characterized in a standard Swagelok two electrode cell configuration in 1 M Na_2SO_4 aqueous electrolyte. One piece of NDC negative electrode and one piece of MnO_2 or Bi^{3+}-modified MnO_2 positive electrode were immersed into the 1 M Na_2SO_4 aqueous solution. These two electrodes were subsequently assembled together with a separator (normal filter paper) sandwiched in between. For both cyclic voltammetry and charge/discharge tests of full cell, the voltage within the range of 0–2.5 V was used for aqueous electrolyte test. Cyclic voltammetry measurement was performed at various scan rates including 10, 25, 50, 100, and 200 mV s^{-1}, while the galvanostatic charge/discharge measurement was tested at current densities of 1, 2, 5, 10, 20, 30, 40, 50 and 100 A g^{-1}. Electrochemical impedance spectroscopy (EIS) test was measured in the frequency range from 0.01 to 10^5 Hz. The mass loading of NDC is about 2 mg, while the mass loading of MnO_2 or Bi^{3+}-modified MnO_2 is about 1 mg.

[1] G. Wang, L. Zhang, J. Zhang, *Chem. Soc. Rev.* **2012**, *41*, 797–828.
[2] S.-M. Chen, R. Ramachandran, V. Mani, R. Saraswathi, *Int. J. Electrochem. Sci.* **2014**, *9*, 4072–4085.
[3] Z. S. Iro, C. Subramani, S. S. Dash, *Int. J. Electrochem. Sci.* **2016**, *11*, 10628–10643.
[4] T. Zhai, S. Sun, X. Liu, C. Liang, G. Wang, H. Xia, *Adv. Mater.* **2018**, *30*, 1706640.
[5] H. Xia, X. Zhu, J. Liu, Q. Liu, S. Lan, Q. Zhang, X. Liu, J. K. Seo, T. Chen, L. Gu, Y. S. Meng, *Nat. Commun.* **2018**, *9*, 5100.
[6] Q. Chen, S. Sun, T. Zhai, M. Yang, X. Zhao, H. Xia, *Adv. Energy Mater.* **2018**, *8*, 1800054.
[7] T. Brousse, M. Toupin, R. Dugas, L. Athouël, O. Crosnier, D. Bélanger, *J. Electrochem. Soc.* **2006**, *153*, A2171–A2180.
[8] S. Devaraj, N. Munichandraiah, *J. Phys. Chem. C* **2008**, *112*, 4406–4417.
[9] S. Zhu, L. Li, J. Liu, H. Wang, T. Wang, Y. Zhang, L. Zhang, R. S. Ruoff, F. Dong, *ACS Nano* **2018**, *12*, 1033–1042.
[10] N. Jabeen, A. Hussain, Q. Xia, S. Sun, J. Zhu, H. Xia, *Adv. Mater.* **2017**, *29*, 1700804.
[11] T. Xiong, T. L. Tan, L. Lu, W. S. V. Lee, J. Xue, *Adv. Energy Mater.* **2018**, *8*, 1702630.
[12] M. Huang, F. Li, F. Dong, Y. X. Zhang, L. L. Zhang, *J. Mater. Chem. A* **2015**, *3*, 21380.
[13] W. Guo, C. Yu, S. Li, Z. Wang, J. Yu, H. Huang, J. Qiu, *Nano Energy* **2019**, *57*, 459–472.
[14] E. Silvester, A. Manceau, V. A. Drits, *Am. Mineral.* **1997**, *82*, 962–978.
[15] S. Ching, D. J. Petrovay, M. L. Jorgensen, S. L. Suib, *Inorg. Chem.* **1997**, *36*, 883–890.
[16] M. Yao, X. Ji, T.-F. Chou, S. Cheng, L. Yang, P. Wu, H. Luo, Y. Zhu, L. Tang, J. Wang, M. Liu, *ACS Appl. Energy Mater.* **2019**, *2*, 2743–2750.
[17] X. Zhang, M. He, P. He, C. Li, H. Liu, X. Zhang, Y. Ma, *Appl. Surf. Sci.* **2018**, *433*, 419–427.
[18] S. Zhu, W. Huo, X. Liu, Y. Zhang, *Nanoscale Adv.* **2019**, DOI: 10.1039/C9NA00547A.
[19] C. C. Ji, M. W. Xu, S. J. Bao, C. J. Cai, R. Y. Wang, D. Z. Jia, *J. Solid State Electrochem.* **2013**, *17*, 1357.
[20] J. Morgan, W. Stumm, *J. Colloid Sci.* **1964**, *19*, 347.
[21] J. W. Murray, *J. Colloid Interface Sci.* **1974**, *46*, 357–371.
[22] S. Zhao, T. Liu, M. S. Javed, W. Zeng, S. Hussain, Y. Zhang, X. Peng, *Electrochim. Acta* **2016**, *191*, 716–723.
[23] R. Inoue, M. Nakayama, *ECS Trans.* **2010**, *25*, 71–78.
[24] L. Liu, M. Min, F. Liu, H. Yin, Y. Zhang, G. Qiu, *J. Power Sources* **2015**, *277*, 26–35.
[25] H. Liu, W. Gu, B. Luo, P. Fan, L. Liao, E. Tian, Y. Niu, J. Fu, Z. Wang, Y. Wu, G. Lv, L. Mei, *Electrochim. Acta* **2018**, *291*, 31–40.
[26] H. Peng, H. Fan, M. Zhang, L. Ning, *Appl. Phys. A* **2018**, *124*, 482.
[27] N. Jabeen, A. Hussain, Q. Xia, S. Sun, J. Zhu, H. Xia, *Adv. Mater.* **2017**, *29*, 1700804.
[28] T. Xiong, W. S. V. Lee, J. Xue, *ACS Appl. Energy Mater.* **2018**, *1*, 5619–5626.
[29] T. Xiong, T. L. Tan, L. Lu, W. S. V. Lee, J. Xue, *Adv. Energy Mater.* **2018**, *8*, 1702630.
[30] S. Zhao, T. Liu, D. Hou, W. Zeng, B. Miao, S. Hussain, X. Peng, M. S. Javed, *Appl. Surf. Sci.* **2015**, *356*, 259–265.
[31] F. K. Ojebuoboh, *JOM.* **1992**, *44*, 46–49.
[32] H. Sun, L. Zhang, K. Y. Szeto, *Met. Ions Biol. Syst.* **2004**, *41*, 333–378.
[33] A. C. Thenuwara, S. L. Shumlas, N. H. Attanayake, Y. V. Aulin, I. G. McKendry, Q. Qiao, Y. Zhu, E. Borguet, M. J. Zdilla, D. R. Strongin, *ACS Catal.* **2016**, *6*, 7739–7743.
[34] F. Dong, T. Xiong, Y. Sun, H. Huang, Z. Wu, *J. Mater. Chem. A* **2015**, *3*, 18466–18474.
[35] H. Yu, L. Shang, T. Bian, R. Shi, G. I. N. Waterhouse, Y. Zhao, C. Zhou, L.-Z. Wu, C.-H. Tung, T. Zhang, *Adv. Mater.* **2016**, *28*, 5080–5086.
[36] U. N. Maiti, W. J. Lee, J. M. Lee, Y. Oh, J. Y. Kim, J. E. Kim, J. Shim, T. H. Han, S. O. Kim, *Adv. Mater.* **2014**, *26*, 40–67.
[37] D. Wang, Y. Chen, H. Wang, P. Zhao, W. Liu, Y. Wang, J. Yang, *Appl. Surf. Sci.* **2018**, *457*, 1018–1024.
[38] Y. F. Yao, N. Gupta, H. S. Wroblowa, *J. Electroanal. Chem.* **1987**, *223*, 107–117.
[39] C. Xia, Q. Jiang, C. Zhao, M. N. Hedhili, H. N. Alshareef, *Adv. Mater.* **2016**, *28*, 77–85.
[40] S. Rodrigues, N. Munichandraiah, A. K. Shukla, *J. Power Sources* **2000**, *87*, 12–20.
[41] T. Xiong, Z. G. Yu, W. S. V. Lee, J. Xue, *ChemSusChem* **2018**, *11*, 3307–3314.
[42] J. P. Perdew, K. Burke, M. Ernzerhof, *Phys. Rev. Lett.* **1996**, *77*, 3865.
[43] P. E. Blöchl, *Phys. Rev. B* **1994**, *50*, 17953.
[44] G. Kresse, J. Furthmüller, *Comput. Mater. Sci.* **1996**, *6*, 15.
[45] G. Henkelman, A. Arnaldsson, H. Jónsson, *Comput. Mater. Sci.* **2006**, *36*, 354.